AIAA JOURNAL
Vol. 40, No. 9, September 2002

Vibrational Excitation, Thermal Nonuniformities, and Unsteady Effects on Supersonic Blunt Bodies

Graham V. Candler*
University of Minnesota, Minneapolis, Minnesota 55455
J. Daniel Kelley†
Stanford University, Stanford, California 94305
Sergey O. Macheret‡ and Mikhail N. Shneider§
Princeton University, Princeton, New Jersey 08544
and
Igor V. Adamovich¶
The Ohio State University, Columbus, Ohio 43210

We have performed a computational study of the experiments performed by Lowry et al. at the Arnold Engineering Development Center. In these experiments, an rf discharge is used to weakly ionize a volume of air; then a projectile is fired through this plasma. Relative to the conditions without the discharge, the shock standoff distance is observed to increase substantially, and the bow shock becomes flatter. We have modeled the rf discharge and the resulting thermochemical state of the air within the discharge region. Based on these conditions, the projectile flowfield was simulated to determine whether the relaxation of the stored internal energy causes the observed shock movement. The results indicate that the stored internal energy does not relax fast enough to reproduce the experimental results, and, therefore, vibrational energy storage is not responsible for the observed shock movement. We consider two additional mechanisms to explain the experiments: modification of the electric field by the presence of the metallic projectile, and thermal nonuniformities in the plasma. The latter effect appears to provide the best explanation for the observations. We have also modeled experiments in which microwave-discharge excited air flows over a model. Unsteady thermal effects in the pulsed discharge can account for most of the observed drag change.

Introduction

A SERIES of experiments at the Arnold Engineering Development Center (AEDC) has been carried out over the past several years.[1,2] This work was originally planned to reproduce experiments performed in Russia that showed significant increases in shock standoff distances on spheres flying through a weakly ionized gas.[3,4] In the AEDC experiments, an rf plasma generator similar to that used in the Russian experiments was installed in the AEDC S1 Hypervelocity Impact Range. Spheres of $\frac{3}{8}$- and $\frac{3}{4}$-in. (0.95- and 1.90-cm) diam were fired through air and argon at pressures of 30 and 40 torr (4000 and 5300 Pa). The bow shock shape was measured with holographic interferometry methods, and the temperature within the discharge was measured with a variety of techniques. Figure 1 shows a schematic of the rf plasma generator used in the experiments, and Fig. 2 shows pictures of the generator operating in argon. The glowing regions indicate the primary current carrying paths of the plasma; note that there is substantial nonuniformity within the generator. The bow shock shape is measured when the projectile is nominally centered in the generator.

The AEDC experiments show that the bow shock tends to flatten and its standoff distance increases when the plasma generator is turned on. There is a substantial amount of scatter of the data, but in air the shock standoff distance Δ is measured to be up to $\Delta/r_n = 0.63$, where r_n is the projectile radius. This compares to the shock standoff distance of $\Delta/r_n = 0.31$ for a sphere flying through air at the range conditions using the average measured temperature of 1156 K. Thus, the change in the standoff distance is substantial and cannot be explained by simple thermal effects.

Candler and Kelley[5,6] modeled the AEDC experiments by assuming that the excited gas within the discharge region was heated and vibrationally excited by the discharge. In addition, it was assumed that several percent of the oxygen was dissociated by the discharge. As the gas flows over the model, the vibrational energy relaxes, releasing heat and increasing the local speed of sound. This results in a reduction of the effective Mach number and, therefore, an increase in the shock standoff distance.

The assumed levels of vibrational excitation and oxygen dissociation were varied parametrically to determine if a reasonable level of excitation could reproduce the experiments. It was found that, if the vibrational energy is characterized by a temperature of 8000 K, and there is a 3% O-atom mole fraction, the computations could reproduce the experiments. This agreement may be completely fortuitous because no attempt was made to relate the assumed internal energy state to the actual plasma conditions.

In this work, we undertake a complete modeling of the rf discharge used in the AEDC experiments to determine the internal energy state under the experimental conditions. The results of this modeling are then used as input to the computational fluid dynamics code used in the previous study to determine if internal energy relaxation causes the observed shock motion.

Modeling calculations have been done in three stages. First, a one-dimensional rf discharge code was used to determine the electric field in the positive column of the discharge, taking into account the voltage drops across the dielectric layers covering the electrodes as well as across the sheaths. Second, a time-dependent vibrational kinetics/air chemistry code was used to determine the quasi-steady-state chemical composition and vibrational energy balance in the rf discharge plasma. Calculations were made for three values of the

Received 23 November 2001; revision received 20 February 2002; accepted for publication 11 March 2002.

*Professor, Department of Aerospace Engineering and Mechanics, 110 Union Street SE; candler@aem.umn.edu. Associate Fellow AIAA.
†Visiting Scholar, Mechanical Engineering Department. Member AIAA.
‡Senior Research Scientist, Department of Mechanical and Aerospace Engineering. Associate Fellow AIAA.
§Research Staff Member, Department of Mechanical and Aerospace Engineering. Member AIAA.
¶Associate Professor, Department of Aerospace Engineering and Aviation. Associate Fellow AIAA.

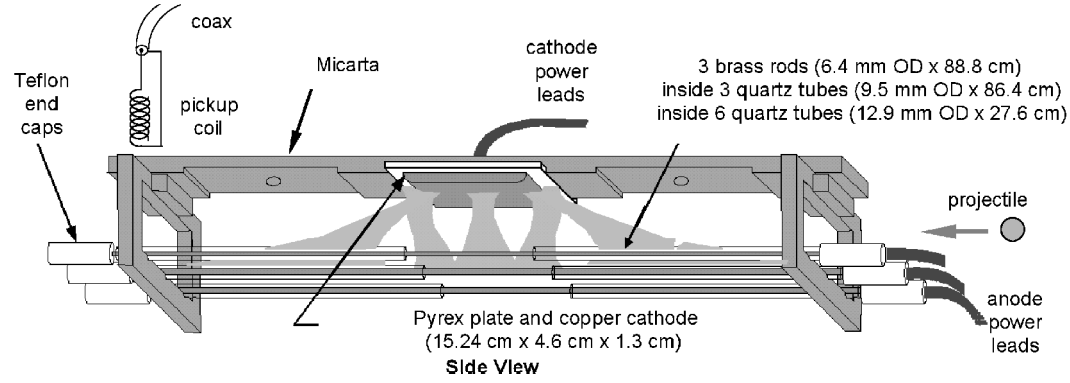

Fig. 1 Schematic of the AEDC rf plasma generator (courtesy of Heard Lowry, Sverdrup/AEDC).

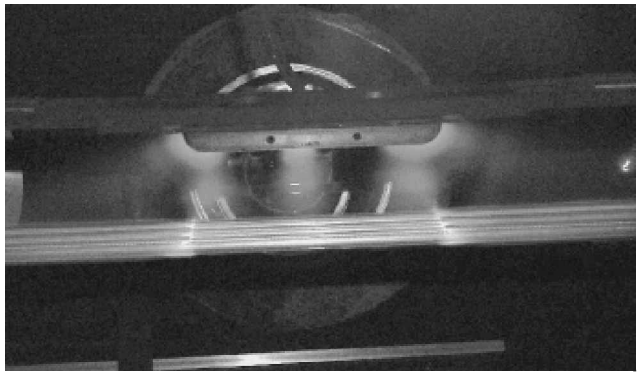

Fig. 2 AEDC rf plasma generator under operating conditions in argon (courtesy of Heard Lowry, Sverdrup/AEDC).

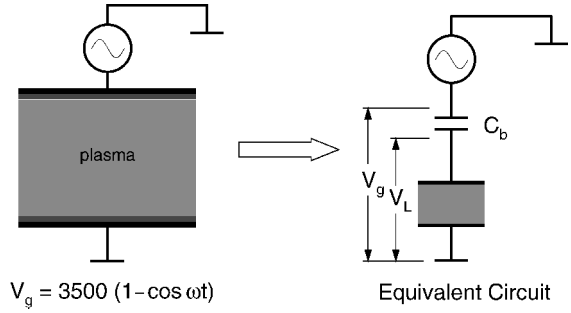

Fig. 3 Equivalent circuit model of the rf plasma generator.

effective ionization rate constant, calculated separately for regular air and for air with 1 and 3% of NO, respectively. This allowed incorporating the effect of the chemical composition change on the ionization rate in the rf discharge model. Finally, the results of the time-dependent model were averaged over a time period and used as input to the finite rate thermochemistry computational fluid dynamics (CFD) code to predict the modification of the flowfield.

Radio Frequency Discharge Model

The rf discharge is modeled through the use of an equivalent circuit, as shown in Fig. 3. The voltage drop across the dielectric layers covering the electrodes, as well as across the sheaths, is modeled. Then we solve the following one-dimensional continuity equations for the electron density n_e and positive ion density n_+; in addition, the Poisson equation for the potential ϕ is solved:

$$\frac{\partial n_e}{\partial t} + \frac{\partial \Gamma_e}{\partial x} = \alpha|\Gamma_e| - \beta n_e n_+, \qquad \Gamma_e = -\mu_e n_e E$$

$$\frac{\partial n_+}{\partial t} + \frac{\partial \Gamma_+}{\partial x} = \alpha|\Gamma_e| - \beta n_e n_+, \qquad \Gamma_+ = \mu_+ n_+ E$$

$$\frac{\partial^2 \phi}{\partial x^2} = -\frac{e}{\epsilon_o}(n_+ - n_e), \qquad E = -\frac{\partial \phi}{\partial x}$$

$$-\int_0^L E(x,t)\,\mathrm{d}x = V_L(x,t) = V_g - \frac{Q}{C_b}$$

where Q is the electric charge on the effective ballast capacitor with capacitance C_b, and $V_g = 3500(1 - \cos \omega t)$ V is the imposed voltage of the rf generator operating at frequency ω; α is the Townsend ionization coefficient, which for $E/N < 100$ Td is taken from the Boltzmann equation solver to be discussed in the next section. For $E/N > 100$ Td, α is taken from Ref. 7 ($1\ \mathrm{Td} = 10^{-17}\ \mathrm{V \cdot cm^2}$). The electron–ion recombination coefficient is β, which is taken to be[7] $\beta = 2 \times 10^{-7}\sqrt{(300/T_e)}\ \mathrm{cm^3/s}$, with T_e, the electron temperature, in degrees Kelvin. The electron temperature and mobilities, μ_e and μ_+, are also obtained from the Boltzmann solver.

$I = \partial Q/\partial t$ is the current in the external circuit. For a symmetric rf discharge, $I(t) = \{\epsilon_o \partial E(x,t)/\partial t + e[\Gamma_+(x,t) - \Gamma_e(x,t)]\}S$, where S is the surface area of the electrodes. In the rf discharge, the boundary conditions on the dielectric surfaces are the same as on metal electrodes. At $x = 0$,

$$\Gamma_e = -\gamma\Gamma_+ \qquad \text{if} \qquad E(0,t) \le 0$$

$$\Gamma_+ = 0 \qquad \text{if} \qquad E(0,t) > 0$$

where γ is the effective secondary emission coefficient from the electrode, which is taken to be 0.01 in this work.[8] At $x = L$, the boundary conditions are similar. The solution of these equations yields the time-dependent variation of the voltage, current density, and reduced field in the rf discharge region.[9] For example, Fig. 4 plots the results of a sample calculation.

Vibrational Kinetics and Air Chemistry Model

The results of the discharge modeling are used to predict the vibrational and chemical state of the air within the discharge. The kinetic model used and the nonequilibrium air chemistry computer code incorporate electron impact processes, vibrational relaxation by vibration–translation (V–T) and vibration–vibration (V–V) processes, and chemical reactions including dissociation and the Zeldovich reactions. The rates of electron impact processes used by the code are evaluated separately using a Boltzmann equation solver.[10] To estimate the effect of the plasma chemical composition on the electron kinetics, these rates have been evaluated for two different gas mixtures, air and air +1% nitric oxide. The rate constants for the V–T and V–V processes, as well as the chemical reaction rate constants, are taken from Ref. 11. For convenience, the V–T and V–V rate constants used are given in the Appendix.

The vibrational kinetics and chemistry model incorporates three equations for the vibrational energy modes of N_2, O_2, and NO, respectively (based on the harmonic oscillator approximation). The quasi-steady-state concentrations of electronically excited species in the rf discharge are calculated to be quite small, and, therefore, the enthalpy stored in these species is negligible.

In the absence of the gas flow in the rf discharge, the dominant cooling mechanism is by natural convection, which cannot be modeled with the one-dimensional approach used here. For

Table 1 Predicted quasi-steady-state rf discharge plasma conditions

T, K	Gas	$T_{v\mathrm{N_2}}$, K	$T_{v\mathrm{O_2}}$, K	% O	% NO
1100	Air	2270	1140	1.20	0.64
1100	Air + 1% NO	2260	1140	0.95	0.48
1600	Air	2080	1615	2.46	0.20
1600	Air + 1% NO	2090	1615	2.01	0.15

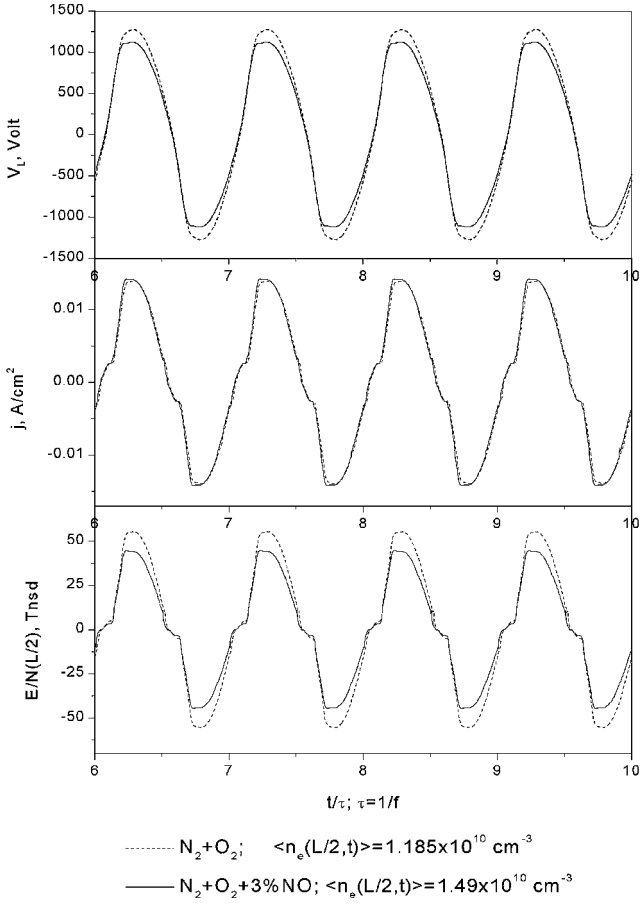

Fig. 4 Voltage on the plasma gap; current density and reduced electric field in the middle of the gap for $T = 1150$ K, $p = 30$ torr, $\gamma = 0.01$, $f = 369$ kHz, $C_b = 1.76 \times 10^{-12}$ F/cm^2, and $L = 6$ cm.

this reason, the gas temperature is assumed to be constant. In the calculations, two values of the gas temperature have been used, $T = 1100$ and 1600 K, which correspond to the average and the maximum values of the temperature measured in the AEDC experiments. The calculated time-averaged electron density is in the range $n_e = (1.2 - 1.5) \times 10^{10}$ cm^{-3}, which is consistent with the experimental value of $n_e = 0.8 \times 10^{10}$ cm^{-3}.

The electron energy relaxation time at the conditions of the AEDC experiments is shorter than the rf oscillation period, so that T_e (or, more exactly, the electron energy distribution function) oscillates with the field. Because of this, the vibrational kinetics and chemistry code had to be run until quasi-steady-state conditions were reached, which typically required about 0.2 s, or 10^5 electric field oscillation periods. The results are summarized in Table 1. Calculations show that the vibrational mode temperatures and the chemical composition of the plasma are primarily controlled by the V–T relaxation of N_2 and O_2 by O atoms, as well as by the N_2–NO and N_2–O_2 V–V exchanges. In particular, nitric oxide is mostly formed by Zeldovich mechanism reactions at the transient, highly nonequilibrium stage of the discharge development. The overshoot of the vibrational temperature of N_2, as well as the steady-state NO concentration, are very sensitive to the N_2–NO V–V and N_2–O V–T rates. On the other hand, the steady-state O atom concentration is much less sensitive to the V–T and V–V rates because O atoms are predominantly formed by the electron impact dissociation and thermal dissociation of O_2 (at the higher gas temperature). In all calculated regimes, the fast O_2–O V–T rate ensures that the vibrational temperature of O_2 is very close to the gas temperature.

CFD Model

The results of the rf discharge modeling were used as freestream conditions for CFD simulations of the AEDC spherical projectiles. Rather than solving for the vibrational temperatures of the gas, a vibrational state-specific model is used. We use five vibrational levels each for N_2 and O_2 and two vibrational levels for NO. In addition, we include the presence of O atoms. Each of the vibrational species interact with each other through the V–T and V–V relaxation processes. Here, we include only the dominant mechanisms, which are O_2 dissociation and recombination, N_2 V–T relaxation on O atoms, O_2 V–T relaxation on all species, NO V–T relaxation on all species, N_2–NO V–V relation, O_2–NO V–V relaxation, and N_2–O_2 V–V relaxation. These processes and the relevant rate constants are given in the Appendix. This model is fully consistent with that used by the one-dimensional Boltzmann solver that was used to obtain the vibrational and chemical state of the discharge.

The conservation equations for this gas mixture are solved on a finite volume grid of 100×200 cells for the forebody of a spherical projectile using a standard CFD method.[12] Figure 5 shows a typical grid; note that the upstream edge of the grid has $x = \text{const}$. This is for convenience in the studies discussed hereafter.

In all calculations presented here, we simulated a $\frac{3}{4}$-in. (1.90-cm)-diam projectile traveling at a speed of 1600 m/s and a freestream pressure of 30 torr (4000 Pa). Figure 6 plots the temperature along

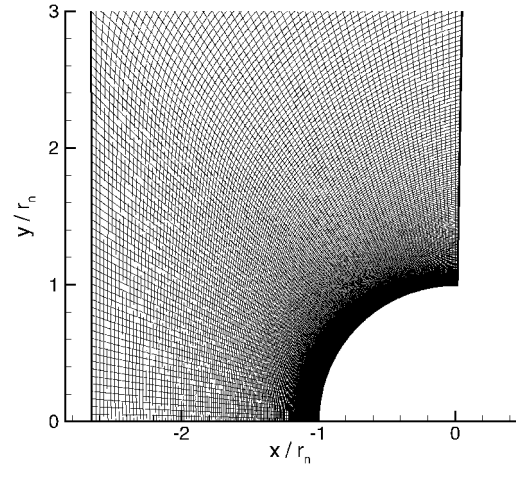

Fig. 5 Example computational 100 (axial) × 200 (normal) point grid.

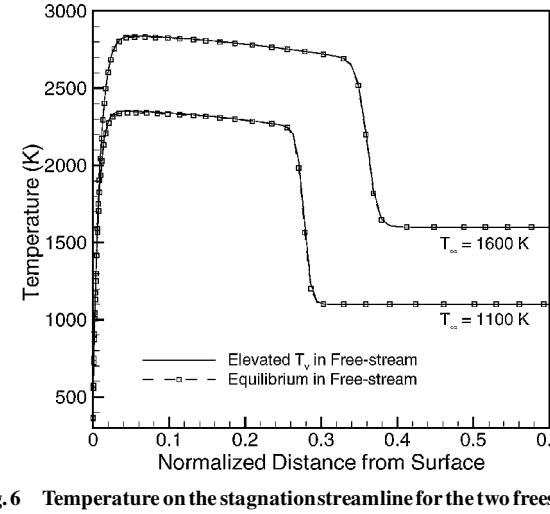

Fig. 6 Temperature on the stagnation streamline for the two freestream temperatures.

the stagnation streamline for the two assumed temperature conditions (1100 and 1600 K). We see that, when the freestream vibrational energy is elevated to the values in Table 1, there is essentially no shock movement. Note that the maximum experimentally measured normalized shock distance was 0.63, which is much larger than any of the computed values. The N_2 vibrational energy does not relax as the gas passes through the flowfield because the relaxation rates are relatively slow. There is appreciable O_2 relaxation, but because its vibrational temperature is only slightly elevated above the freestream, the relaxation has little effect. There is little or no energy release due to O atom recombination, again due to relatively slow rates.

The lack of shock movement is, therefore, a result of very little relaxation of N_2 and essentially no nonequilibrium excitation of O_2. This can be seen in Figs. 7 and 8, which plot the mass fractions of the N_2 and O_2 vibrational states along the stagnation streamline for the two assumed freestream temperatures. Note that the mass fractions of the N_2 vibrational species do not change appreciably, whereas the O_2 upper levels start to increase at the shock. Thus, N_2 relaxes too slowly to deposit energy into the flowfield, and O_2 is too weakly excited to have any substantial effect. These results show that the predicted levels of internal energy excitation are insufficient to explain the experiments.

The question now remains: If it is not vibrational relaxation, what is it? In the remainder of the paper, we discuss two possible mechanisms: modification of the discharge due to the presence of the metallic projectile and plasma thermal nonuniformities.

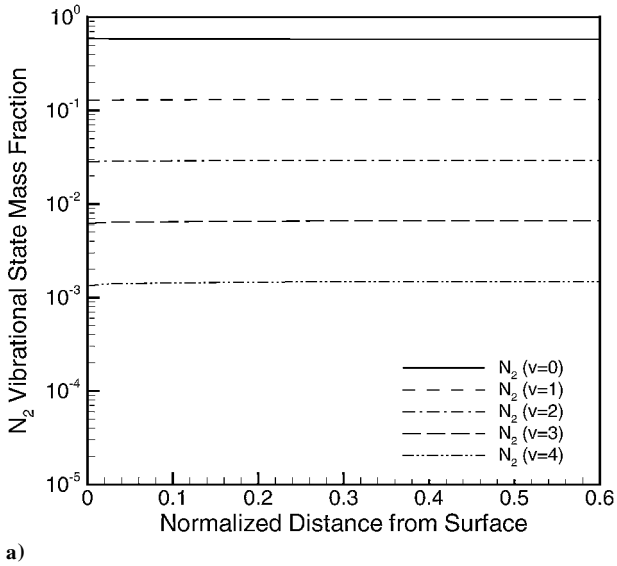

a)

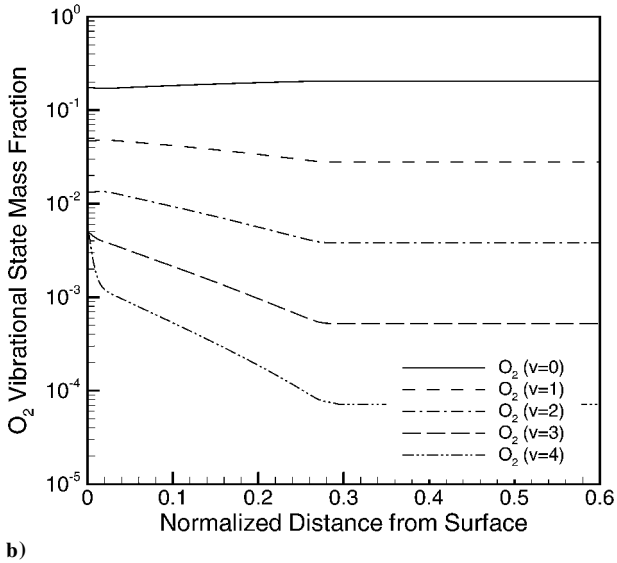

b)

Fig. 7 Computed vibrational state mass fractions on the stagnation streamline for the 1100 K freestream conditions: a) N_2 and b) O_2.

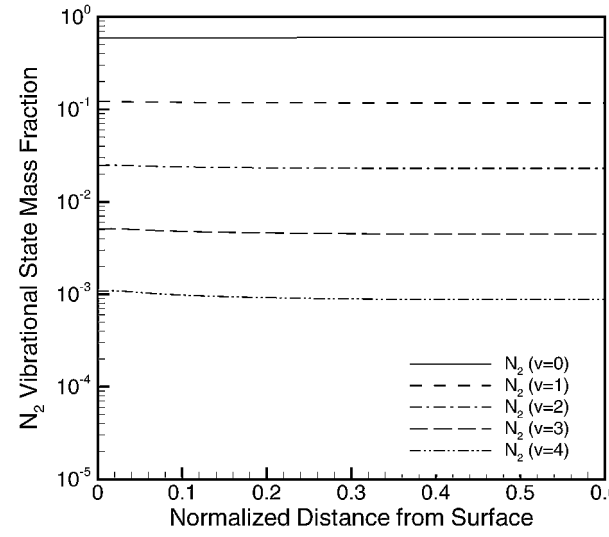

a)

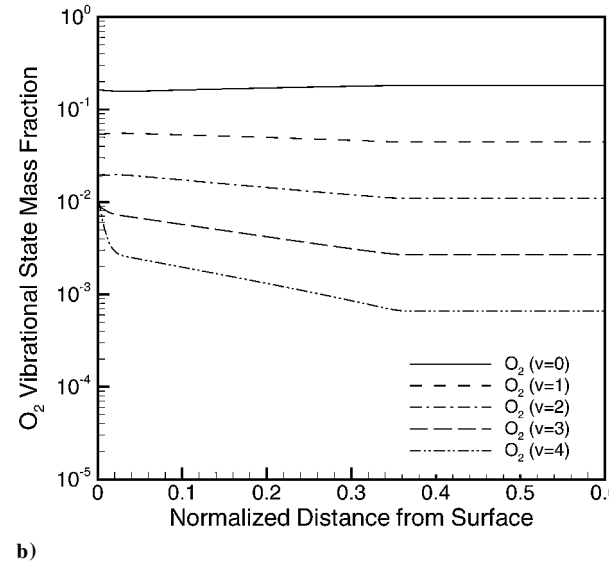

b)

Fig. 8 Computed vibrational state mass fractions on the stagnation streamline for the 1600 K freestream conditions: a) N_2 and b) O_2.

Modification of Discharge

As the metallic spherical projectile passes through the rf plasma generator, it may change the discharge properties. In essence, the sphere acts like an electrode in this rf discharge, which causes a concentration of the current density and field near the sphere. This results in higher Joule heating near the sphere, which may account for the shock motion.

Complete modeling of the interaction of the projectile with the plasma generator in operation would be extremely difficult. One complication is that the AEDC plasma generator has a relatively low frequency of 369 kHz, which means that the sphere travels about 0.43 cm during each cycle. Therefore, it may not be possible to decouple the interaction between the flowfield and the alteration of the discharge by the projectile.

Rather than attempting to model this complex interaction, we used a highly idealized model to assess its importance. We assume that as the projectile flies through the generator, the field is concentrated around the sphere. This results in increased Joule heating in concentric shells around the projectile. For simplicity, we assume that an equal amount of energy is deposited in each spherical shell and that 30% of 3.5 kW generator power goes directly into heating the gas.

Figure 9 plots the shock standoff distance as a function of time for this highly simplified model at a freestream temperature of 1100 K. We observe some shock movement, but it is less than 4% for this case. Although this is larger than the shock movement that can be

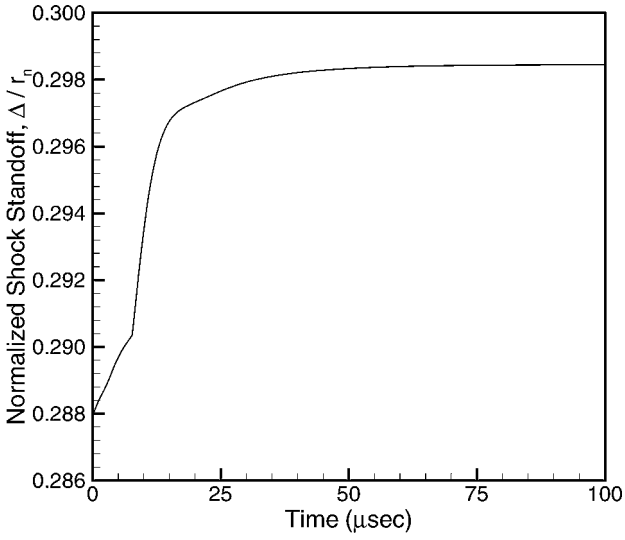

Fig. 9 Shock standoff distance as a function of time for simplified modified discharge model at 1100 K conditions.

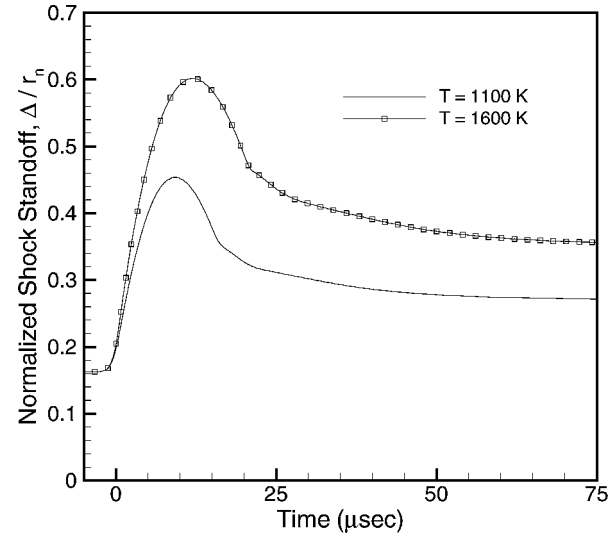

Fig. 10 Shock standoff distance as a function of time for projectile traveling from $T = 300$ K into high-temperature gas at $t = 0$ (either 1100 or 1600 K conditions).

attributed to vibrational energy storage, it is not sufficient to explain the experiments.

This result is consistent with the small projectile residence time within the generator. For a characteristic dimension of the generator of 30 cm, the residence time is 188 μs. The generator deposits less than 1 J of energy during this time, which is not enough to raise the temperature appreciably. Thus, from our simple model and from simple scaling arguments, it is unlikely that the observed shock motion is caused by localized heating due to changes in the discharge.

Plasma Nonuniformities

In this section, we consider how thermal nonuniformities in the plasma may affect the bow shock standoff distance and shape. Figure 2 shows that the plasma is substantially nonuniform, with three glowing regions where the gas is presumably hotter than the mean. This presumption is supported by the temperature measurements made by Lowry et al.[1] in air. The exact variation of the temperature within the generator is impossible to model, and so here we consider several limiting cases to determine how this type of thermal nonuniformity affects the bow shock.

First, consider the simple case where the projectile is flying through uniform air at 300 K and then suddenly enters a region of elevated temperature of either 1100 or 1600 K. To model this computationally, we obtain a converged flow solution at the 300 K conditions and a projectile speed of 1600 m/s. We then introduce high-temperature gas at the upstream edge of the computational domain and use a small time step to obtain a time-accurate simulation of the resulting flowfield. Because the upstream edge of the grid has a constant x location, the inflow gas enters the domain uniformly (Fig. 5).

Figure 10 plots the shock standoff distance as a function of time, where $t = 0$ is taken as the time when the leading edge of the projectile encounters the high-temperature gas. We see that there is a significant overshoot in the shock standoff distance when the hot gas interacts with the bow shock. This begins at a slightly negative time because the shock is upstream of the leading edge. The shock standoff distance increases to $\Delta/r_n = 0.408$ for $T = 1100$ K and $\Delta/r_n = 0.578$ for $T = 1600$ K. The shock standoff distance then decays and eventually reaches its steady-state value for the imposed higher temperature. The maximum shock standoff distance occurs at $t = 8.2$ μs at 1100 K and 10.8 μs at 1600 K. These times are similar to the characteristic flow time, which can be defined as the time it takes the projectile to travel one diameter: $2r_n/u_\infty = 11.9$ μs.

Figure 11 plots the density contours at the time of maximum shock standoff distance for the two cases. We see that, at this condition, the high-temperature gas piles up in front of the original

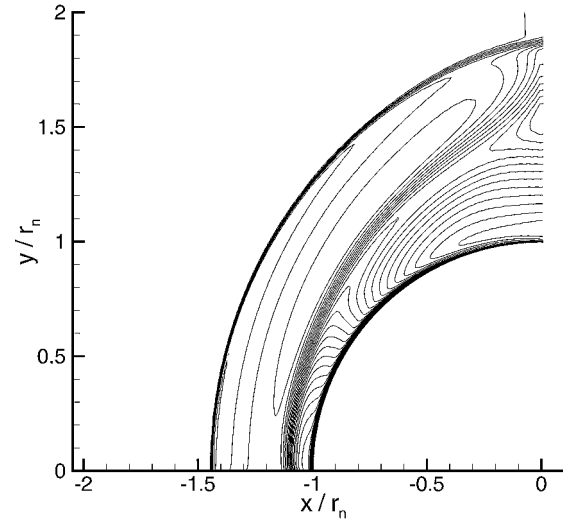

a)

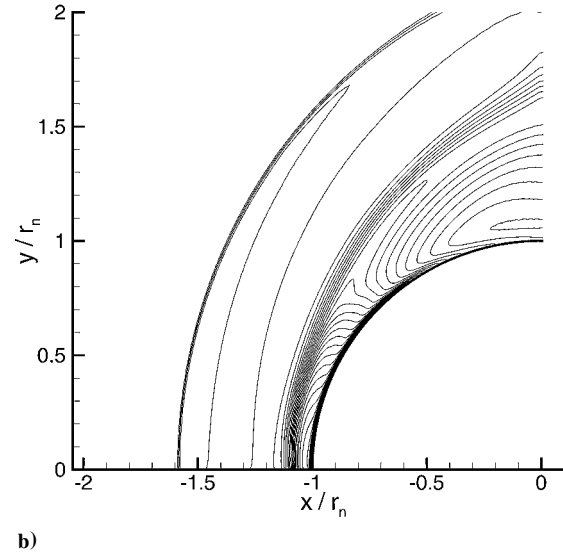

b)

Fig. 11 Density contours at maximum shock standoff distance overshoot for projectile from $T = 300$ K into a) 1100 K gas (at $t = 8.2$ μs) and b) 1600 K gas (at $t = 10.8$ μs).

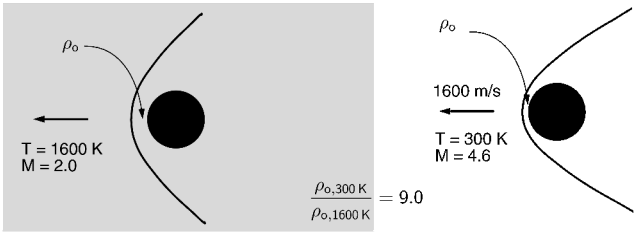

Fig. 12 Schematic representation of stagnation region densities for the conditions corresponding to the AEDC experiments for an assumed discharge temperature of 1600 K.

shock wave, creating a weaker secondary shock and an apparently higher shock standoff distance. This occurs primarily because the high-temperature gas has a significantly lower density than the 300 K gas. Also, the Mach number of the projectile in the high-temperature stream is much lower ($M_\infty = 2.00$ at 1600 K vs 4.60 at 300 K). As a result, the stagnation pressure and temperature in the cold gas are much higher: For example, at $T = 1600$ K, $p_{o,300\ K}/p_{o,1600\ K} = 4.9$, and $\rho_{o,300\ K}/\rho_{o,1600\ K} = 9.0$. Therefore, to the low-density high-temperature gas, the original cold-gas stagnation region is like an immovable object that is actually expanding outward into the lower pressure gas. Of course, this high-pressure gas also flows downstream, draining the stagnation region. This difference in the stagnation region densities is illustrated schematically in Fig. 12.

Another way to think of the flow is that the hot gas has a lower mass flux and momentum flux, which cause the bow shock wave to move upstream to adjust to the new inflow conditions. At the same time, the high-density gas remaining in the stagnation region flows downstream. Thus, there is a balance between the rate at which the new inflow gas encounters the bow shock, the rate at which the bow shock expands, and the rate at which the stagnation region is emptied of high-density gas. These calculations are consistent with previous work in which a projectile flying through a heated gas was analyzed in experiments[13] and calculations.[14]

When the slug of high-temperature gas interacts with the curved bow shock, a baroclinic torque is generated. Consider the two-dimensional compressible Euler equation for the z-direction (out-of-plane) vorticity

$$\frac{\mathrm{D}\omega_z}{\mathrm{D}t} = -\omega_z\left(\frac{\partial u}{\partial x} + \frac{\partial v}{\partial y}\right) - \left(\nabla\frac{1}{\rho} \times \nabla p\right)_z$$

The high-temperature flow has a low density, so that the gradient of $1/\rho$ is in the negative x direction. The gradient of pressure across the shock is in the positive x direction at the centerline and has a negative y component off of the centerline. Therefore, the baroclinic torque tends to produce a negative vorticity away from the axis, which would tend to cause the bow shock to become more curved. The baroclinic torque competes with the effect of compression, which has a positive sign across the shock. However, based on the timescales and Fig. 11, these processes are not responsible for the initial standoff distance overshoot.

In any case, it is clear that the effect of thermal nonuniformities is to cause an unsteady overshoot in the shock standoff distance when the projectile transitions from low- to high-temperature regions. This process occurs on a timescale that is consistent with the timescales of the projectile motion in the AEDC experiments.

Argon Experiments

The AEDC group also performed ballistic range experiments in argon and found significantly less change in the shock shape and standoff distance.[2] Standoff distance ratios of between 0.22 and 0.28 were measured, as compared to a ratio of 0.24 with no plasma. This small shock movement was attributed to the lack of vibrational excitation of argon as opposed to air.[2] However, with the new calculations presented in this report, we must reassess this conclusion.

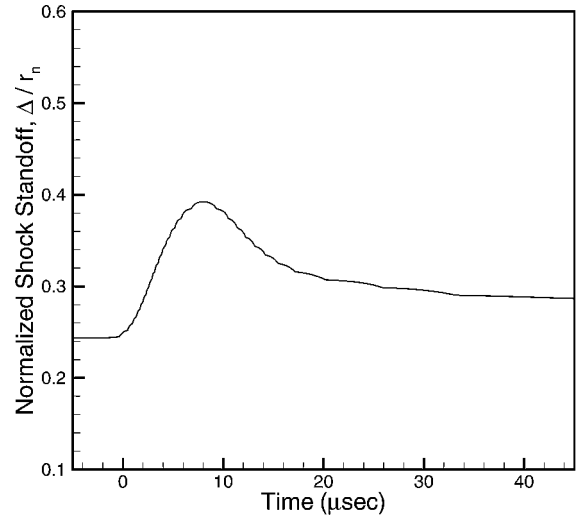

Fig. 13 Shock standoff distance as a function of time for projectile traveling from $T = 300$ K into 650 K argon.

We performed simulations of a nonuniform temperature distribution for the argon experiment in the same fashion as that described earlier for air. We use the appropriate properties for argon and use the estimated temperature in the discharge region of 650 K. Figure 13 plots the variation of the shock standoff distance ratio as a function of time. We see that before entering the high-temperature gas, the shock standoff distance is 0.24, which is consistent with the no-plasma results from the AEDC measurements. The standoff ratio then reaches a maximum of 0.392 at $t = 8.1$ μs, substantially less than the overshoot computed in the air simulations. This result follows from the lower gas temperature in the argon experiments and from the higher ratio of specific heats in argon. These two factors result in a lower stagnation density ratio between the different temperature regions: a stagnation density ratio of just 2.6, as compared to 9.0 in the high-temperature air case. Figure 13 shows that the time to the overshoot is similar to the air simulations, but note that the shock standoff equilibrates to the new value corresponding to $T_\infty = 650$ K much more quickly than in air. This is because the relatively lower density gas is swept downstream more quickly in the argon case.

Pulsed Microwave Experiments

As part of the effort to understand how plasmas affect supersonic aerodynamics, we made an attempt to model the pulsed microwave experiments that have been conducted in Russia over the past several years.[15,16] In these experiments, a microwave[2] discharge excites the supersonic air upstream of a sphere. Relative to the unheated flow conditions, reductions in the drag of 10–15% are measured, and the bow shock standoff distance is observed to increase. Our earlier work attributed the drag reduction to oxygen vibrational relaxation, but we have found that there is insufficient oxygen excitation in these flows to explain the experimental results. Therefore, we investigated the effect of unsteady heating of the gas during the pulsed microwave discharge operation. In the experiments, approximately 0.1 J of heat per 0.2-μs pulse is added to the gas in an imprecisely known volume of a few cubic centimeters.

To model this process, we simulate the flow at conditions characteristic of the experiments and add the heat in various axisymmetrically shaped regions upstream of the model. Figure 14 plots the drag on the sphere as a function of time for three different assumed excitation regions. We see that there is an overshoot and undershoot in the drag coefficient. When we average the typical experimental data over 100 μs, we find that there is a net drag reduction of 5%. This reduction is independent of the assumed energy deposition volume over the range shown in Fig. 14. The reduction is proportional to the added energy. If the first 40–60 μs of the experiment are neglected, the apparent drag reduction can be much larger. Thus, our conclusion is that unsteady heating is consistent with the drag measurements made in this type of experiment.

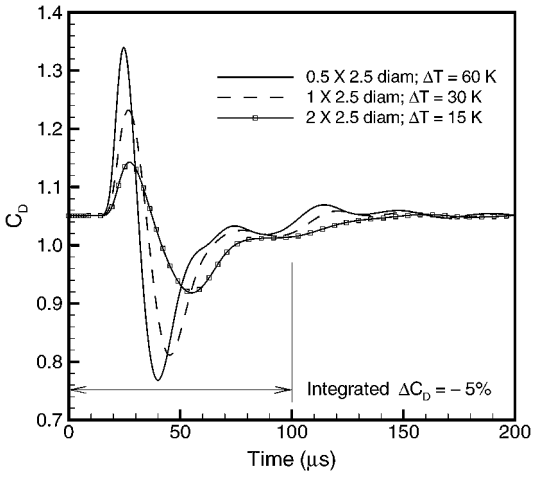

Fig. 14 Drag coefficient as a function of time for three different assumed discharge volumes; freestream conditions are $p_\infty = 60$ torr (8.0 kPa), $T_\infty = 150$ K, and $M_\infty = 1.3$.

Conclusions

The AEDC ballistic range experiments concerning anomalous shock standoff distances have been modeled. A one-dimensional time-dependent model of the rf plasma generator was used to provide voltage, current density, and reduced field data to a Boltzmann solver. This code was used to integrate the plasma properties over many generator cycles until a quasi-steady-state condition was obtained. These results were then used as input to an axisymmetric CFD code. This code uses a vibrational state-specific representation of the gas and includes all relevant vibrational relaxation processes, as well as finite rate oxygen dissociation and recombination.

The results of the modeling the rf plasma generator are that very little vibrational excitation of the gas occurs, with the oxygen vibrational modes only slightly excited over the assumed translational temperature. There is negligible excitation of the electronic states as well. Therefore, when the CFD code is used to simulate the shock standoff distance on the ballistic range projectiles, there is no effect of vibrational relaxation on the shock standoff distance. This is contrasted with the results of Candler and Kelley[5,6] that showed a substantial effect. However, in that work, a high level of vibrational excitation was assumed; based on our current modeling results, that assumption was wrong. Therefore, we must conclude that the observed effects are not a result of vibrational relaxation of stored vibrational energy as postulated previously.

We have considered two possible mechanisms that may be responsible for the experimental observations. First, we considered how the presence of the metallic sphere within the discharge region may affect the gas heating. In particular, we expect that the sphere will act as an electrode during each generator cycle, resulting in localized heating around the sphere. We attempted to assess the importance of the effect using an extremely simplified model; however, this did not produce much change in the shock standoff distance. Also, simple residence time arguments indicate that the plasma generator has insufficient power to change the flowfield appreciably during the passage of the sphere.

The effects of thermal nonuniformities in the plasma were also considered by performing time-dependent simulations of the projectile flying from a cold region (at 300 K) into a hot region (at either 1100 or 1600 K). These calculations show that there is a significant unsteady effect due to the sudden transition; in effect, the hot, low-density gas piles up in front of the original shock layer, resulting in a substantially larger shock standoff distance. For example, for the higher-temperature simulation, the normalized shock standoff increases to a maximum of $\Delta/r_n = 0.60$, which is in the range of the experimental results. Simulations in argon are consistent with the experimental measurements, in that they show much less shock movement due to the lower temperature and different gas properties.

We also performed simulations of pulsed microwave drag reduction experiments. We find that unsteady heat addition causes a temporary drag reduction of a similar magnitude to that measured in recent Russian wind-tunnel experiments. Thus, we find that the observed drag reduction is a thermal effect due to unsteady heating of the gas during the microwave pulse.

Our calculations do not definitively prove that thermal nonuniformities cause the shock movement, but at this point we feel that this is the leading contender for a physically based mechanism to describe the experiments.

Appendix: Relaxation Processes

The V–T relaxation processes[10] are

$$AB(v) + M \rightleftharpoons AB(v-1) + M$$

The rate constants (in units of atmosphere seconds) are, for N_2–N_2, N_2–O_2, and N_2–NO,

$$p\tau_{VT} = \exp\left(234.9T^{-\frac{1}{3}} - 25.89\right)$$

for N_2–O and N_2–N,

$$p\tau_{VT} = \exp\left(32.2T^{-\frac{1}{3}} - 16.35\right)$$

for O_2–O_2, O_2–N_2, and O_2–NO,

$$p\tau_{VT} = \frac{T\exp\left(166.3T^{-\frac{1}{3}} - 33.32\right)}{1 - \exp(-2240/T)}$$

for O_2–O and O_2–N,

$$p\tau_{VT} = \frac{T\exp\left(36.87T^{-\frac{1}{3}} - 27.15\right)}{1 - \exp(-2240/T)}$$

for NO–NO, NO–N_2, and NO–O_2,

$$p\tau_{VT} = \frac{T\exp\left(33.20T^{-\frac{1}{3}} - 25.00\right)}{1 - \exp(-2700/T)}$$

and for NO–O and NO–N,

$$p\tau_{VT} = \frac{3.8 \times 10^{-12}\, T}{1 - \exp(-2700/T)}$$

The V–V relaxation processes[10] are

$$AB(v) + CD(w-1) \rightleftharpoons AB(v-1) + CD(w)$$

The rate constants (in units of cubic centimeters per second) are, for N_2–O_2,

$$k_{10}^{01} = \exp\left(-124.0T^{-\frac{1}{3}} - 22.50\right)$$

for N_2–NO,

$$k_{10}^{01} = \exp\left(-86.35T^{-\frac{1}{3}} - 21.60\right)$$

and for O_2–NO,

$$k_{10}^{01} = \exp\left(-62.46T^{-\frac{1}{3}} - 22.35\right)$$

Acknowledgments

This work was sponsored by the U.S. Air Force Office of Scientific Research, under Grant F49629-00-1-0177. The views and conclusions contained herein are those of the authors and should not be interpreted as necessarily representing the official policies or endorsements, either expressed or implied, of the Air Force Office of Scientific Research or the U.S. Government. This work was also supported in part by the U.S. Army High Performance Computing Research Center under the auspices of the Department of the Army, Army Research Laboratory Cooperative Agreement DAAD191-01-2-0014, the content of which does not necessarily reflect the position or the policy of the U.S. Government, and no official endorsement should be inferred.

References

[1]Lowry, H., Stepanek, C., Crosswy, L., Sherrouse, P., Smith, M., Price, L., Ruyten, W., and Felderman, J., "Shock Structure of a Spherical Projectile in Weakly Ionized Air," AIAA Paper 99-0600, Jan. 1999.

[2]Lowry, H., Smith, M., Sherrouse, P., Felderman, J., Bauer, M., Pruitt, D., and Keefer, D., "Ballistic Range Tests in Weakly Ionized Argon," AIAA Paper 99-4822, Nov. 1999.

[3]Mishin, G. I., Serov, Yu. L., and Yavor, I. P., "Flow Around a Sphere Moving Supersonically in a Gas Discharge Plasma," *Pis'mav Zhurnal Tekhnicheskoi Fiziki (Soviet Technical Physics Letters)*, Vol. 17, June 1991, pp. 65–71.

[4]Bedin, A. P., and Mishin, G. I., "Ballistic Studies of the Aerodynamic Drag on a Sphere in Ionized Air," *Pis'mav Zhurnal Tekhnicheskoi Fiziki (Soviet Technical Physics Letters)*, Vol. 21, Jan. 1991, pp. 14–19.

[5]Candler, G. V., and Kelley, J. D., "Effect of Internal Energy Excitation on Supersonic Air Flow," AIAA Paper 99-4964, Nov. 1999.

[6]Candler, G. V., and Kelley, J. D., "Effect of Internal Energy Excitation on Supersonic Blunt-Body Drag," AIAA Paper 99-0418, Jan. 1999.

[7]Kossyi, I. A., Kostinsky, A. Y., Matveyev, A. A., and Silakov, V. P., "Kinetic Scheme of the Non-Equilibrium Discharge in Nitrogen-Oxygen Mixtures," *Plasma Sources Science and Technology*, Vol. 1, No. 3, 1992, pp. 207–220.

[8]Raizer, Y. P., *Gas Discharge Physics,* Springer, New York, 1997, pp. 73–75.

[9]Raizer, Y. P., Shneider, M. N., and Yatsenko, N. A., *Radio-Frequency Capacitive Discharges*, CRC Press, New York, 1995, pp. 45–55.

[10]Adamovich, I. V., Rich, J. W., and Nelson, G. L., "Feasibility Study of Magnetohydrodynamics Acceleration of Unseeded and Seeded Air Flows," *AIAA Journal*, Vol. 36, No. 4, 1998, pp. 590–597.

[11]Adamovich, I. V., Rich, J. W., Chernukho, A. P., and Zhdanok, S. A., "Analysis of the Power Budget and Stability of High-Pressure Nonequilibrium Air Plasmas," AIAA Paper 00-2418, June 2000.

[12]Wright, M. J., Bose, D., and Candler, G. V., "Data-Parallel Line Relaxation Method for the Navier–Stokes Equations," *AIAA Journal*, Vol. 36, No. 9, 1998, pp. 1603–1609.

[13]Goloviznin, V. P., Mishin, G. I., Serov, Y. L., and Yavor, I. P., "Supersonic Flow Around a Sphere in a Thermal Irregularity," *Zhurnal Tekhnicheskoi Fiziki (Soviet Physics–Technical Physics)*, Vol. 32, No. 7, 1987, pp. 853–855.

[14]Zheleznyak, M. B., Mnatsakanyan, A. K., Pervukhin, S. V., "Unsteady and Nonequilibrium Airflow Near a Stagnation Line," *Izvestiya Akademii Nauk SSSR, Mekhanika Zhidkosti i Gaza (Fluid Mechanics)*, No. 6, 1986, pp. 170–172.

[15]Chuvashev, S. N., Ershov, A. P., Klimov, A. I., Leonov, S. B., Shibkov, V. M., and Timofeev, I. B., "Flow Around Body and Characteristics of AC/DC Discharges in Plasma Aerodynamic Experiment," *Proceedings of the 2nd Weakly Ionized Gases Workshop*, AIAA, Reston, VA, 1998.

[16]Beaulieu, W., Brovkin, V., Goldberg, I., Klimov, A., Kolesnichenko, Y., Krylov, A., Lashov, V., Leonov, S., Mashek, I., Ryvkin, M., and Serov, Y., "Microwave Plasma Influence on Aerodynamic Characteristics of Body in Airflow," *Proceedings of the 2nd Weakly Ionized Gases Workshop*, AIAA, Reston, VA, 1998.

M. Sichel
Associate Editor